ACS APPLIED MATERIALS & INTERFACES

Research Article

www.acsami.org

Ethanol Gas Detection Using a Yolk-Shell (Core-Shell) α-Fe_2O_3 Nanospheres as Sensing Material

LiLi Wang,[†] Zheng Lou,[‡] Jianan Deng,[†] Rui Zhang,[†] and Tong Zhang*[,†]

[†]State Key Laboratory on Integrated Optoelectronics, College of Electronic Science and Engineering, Jilin University, Changchun 130012, PR China

[‡]State Key Laboratory for Superlattices and Microstructures, Institute of Semiconductors, Chinese Academy of Sciences, Beijing 100083, China

Supporting Information

ABSTRACT: Three-dimensional (3D) nanostructures of α-Fe_2O_3 materials, including both hollow sphere-shaped and yolk-shell (core-shell)-shaped, have been successfully synthesized via an environmentally friendly hydrothermal approach. By expertly adjusting the reaction time, the solid, hollow, and yolk-shell shaped α-Fe_2O_3 can be selectively synthesized. Yolk-shell α-Fe_2O_3 nanospheres display outer diameters of 350 nm, and the interstitial hollow spaces layer is intimately sandwiched between the inner and outer shell of α-Fe_2O_3 nanostructures. The possible growth mechanism of the yolk-shell nanostructure is proposed. The results showed that the well-defined bilayer interface effectively enhanced the sensing performance of the α-Fe_2O_3 nanostructures (i.e., yolk-shell α-Fe_2O_3@α-Fe_2O_3), owing predominantly to the unique nanostructure, thus facilitated the transport rate and augmented the adsorption quantity of the target gas molecule under gas detection.

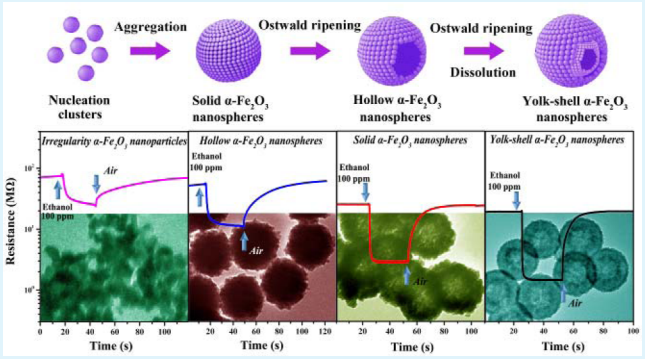

KEYWORDS: *α-Fe_2O_3, yolk-shell nanospheres, porous structure, fast response time, ethanol sensing, gas sensor*

1. INTRODUCTION

The gas sensor is old but perpetual and indeciduous, which now accounts for over 90% of the detection of environmental pollutants.[1] To further satisfy the stringent need for a high-performance gas sensor with the properties of fast response speed, remarkable stability, and excellent selectivity, many researches and creative reforms have been conducted continuously.[2,3] This study not only improves the progress of nanoscience and nanotechnology but also drives economic growth greatly over the past decade. Thus, in order to further cater the technological development requirement, there are increasing demands for designing and engineering new structure nanomaterials. Novel nanostructures such as core-in-hollow-shell, macroporous, multichamber, multishell[4−7] could endow the sensing materials with unconventional functions. For core-in-hollow-shell structure, this kind of material generally can also be regarded as "yolk-shell" structures or "rattle-type" structures.[8,9] Different from the traditional bulk materials, the controllability of the interior-structured to the multilevel scope generally lead to an efficiently increase in catalytic activity because of the larger specific area and a large fraction of the porous structure exposed to the surface.[4,10] Therefore, these vivid yolk-shell (core-shell) structures micro/nanomaterials with a good wealth of outstanding properties can exhibit more space for applications in gas sensors.

Hematite (α-Fe_2O_3) represents a significant class of multifunctional materials and has been widely applying in photocatalysis, lithium batteries, biomedicines, and magnetic devices, especially in sensors.[3,11−13] For example, Sun[14] and Son et al.[15] have successfully applied these yolk-shell Fe_2O_3 particles to lithium-ion batteries. Wang et al.[16] took a template method to synthesize multishelled α-Fe_2O_3 with a hollow interior which revealed enhanced sensing response. Zhang et al.[17] have reported the achievement of multishelled Cu_2O microspheres by a hydrothermal route and show good response to ethanol. Thus, these results ensure that the design of yolk-shell nanostructure of the sensing materials can offer more development space for enhancing sensing performance, which is of large practical and scientific merit.

Herein, yolk-shell (core-shell) α-Fe_2O_3 spheres were obtained by a reproducible, template-free, and one-pot hydrothermal method. By adjusting the reaction time of the precursor, we have achieved α-Fe_2O_3 nanospheres with complex interior structures. Not only the number of shells but also the interior spacing can be regulated. Significantly, α-Fe_2O_3 nanospheres with various interior structures exhibit

Received: May 8, 2015
Accepted: May 26, 2015
Published: May 26, 2015

DOI: 10.1021/acsami.5b03978
ACS Appl. Mater. Interfaces 2015, 7, 13098−13104

distinct differences in sensing performance when applied in the gas sensors.

2. EXERIMENTAL SECTION

2.1. Materials. All the reagents in the experiment were of analysis grade and used without further purification.

2.2. Synthesis Process. *Synthesis of Yolk-Shell (Core-Shell) α-Fe_2O_3 Nanospheres.* α-Fe_2O_3 nanostructures were synthesized followed the reported method with some modification.[18] Brief, 0.25 g of potassium ferricyanide ($K_3[Fe(CN)_6]$) and 0.038 g of ammonium dihydrogen phosphate ($NH_4H_2PO_4$) was dispersed in a certain amount of distilled water to form a suspension solution. After being stirred for 30 min, the above mixture solution was transferred to a Teflon-lined stainless autoclave with a volume of 100 mL, which was then heated at 200 °C for 30 h in an air flow electric oven. Moreover, nanoparticles/solid/hollow-structures of α-Fe_2O_3 materials were obtained by hydrothermal treatment for different reaction times for 0, 1, and 18 h, respectively. Finally, the achieved products were washed with ethanol/water several times before being vacuum-dried at 50 °C.

2.3. Characterization. First, field emission scanning electron microscope (FESEM, FEI Company, XL 30 ESEM FEG) and X-ray diffraction (XRD, λ = 0.15418 nm) analysis were employed to determined the surface morphologies and crystalline phase of the as-synthesized products. The interior structures of the samples were observed by a Tecnai G^2 20S-Twin transmission electron microscope (TEM and HRTEM) operating at an accelerating voltage of 120 and 200 kV. For the TEM and HRTEM tests, the obtained products were first dissolved in an organic solvent (ethanol) via an ultrasonic treatment. Then, a small drop of the above suspension solution was dropped onto a copper grid. Energy-dispersive X-ray (EDX) and the selected area electron diffraction (SAED) were attached on the TEM. Moreover, the Brunauer–Emmett–Teller (BET) specific surface areas and pore size distributions of the as-synthesized products were measured with a Quantachrome NOVA 1000e analyzer.

3. RESULTS AND DISCUSSION

3.1. Structural and Morphological Characteristics. A strategy of preparing the α-Fe_2O_3 samples that is motivated by the yolk-shell nanostructure is revealed in Scheme 1, in combination with FESEM and TEM images of the samples corresponding to each step (Figure 1). It proposes that for the yolk-shell α-Fe_2O_3 samples, a development procedure involves the nucleation process, nanoparticles aggregation, ostwald ripening, and dissolution/ostwald ripening. I step-nucleation process: in its infancy of reaction, a great quantity of primary α-Fe_2O_3 nanoparticles uniformly precipitate from the suspension solution. However, the primary nanoparticles are very unstable in virtue of high surface energy, which results in the aggregation until it attains a thermodynamic steady state. So, the scattered nanoparticles with several nanometers in size are distinctly obtained as an intermediate material at the initial reaction process (Figure 1a,b). II step-aggregation process: During this process, the solid nanospheres are obtained via an oriented attachment aggregation of the neighboring above intermediate nanoparticles. The surface and interior structures of the obtained samples by the aggregation process can be distinctly observed in Figure 1c,d, where with the increase of reaction time above primary nanoparticles (Figure 1a) are aggregating to form solid nanospheres (Figure 1d) with a coarse surface. The diameters of each nanosphere are relatively uniform (110 nm). III step-Ostwald ripening: As the reaction continues, the interior of above solid spheres (II step) have a strong tendency to dissolve, which provides the driving force for the spontaneous insideout Ostwald ripening. Finally, the hollow nanospheres with a diameter of about 120 nm and a thickness of shell layer of about 40 nm (Figure 1e,f) were obtained. IV step-Ostwald ripening and dissolution: Further prolonging the reaction time, a small number of amorphous nanoparticles of hollow nanospheres inner shell start to ripen and crystallize around the inner-surface to form double-shell spheres. Phosphate ions, as a ligand, can react with α-Fe_3O_2 to form the coordination effect, result in enhacing the dissolution process (eq 1).[19]

$$\alpha\text{-}Fe_2O_3 + 2xH_2PO_4^- + 6H^+ \rightarrow 2[Fe(H_2PO_4)_x]^{3-x} + 3H_2O \quad (1)$$

Finally, the synergistic effect of Ostwald ripening process and dissolution process lead to formation of the yolk-shell nanospheres (Figure 1g,h). We deduced from the above

Scheme 1. Schematic Illustration of the Synthetic Route to Yolk-Shell α-Fe_2O_3 Nanospheres

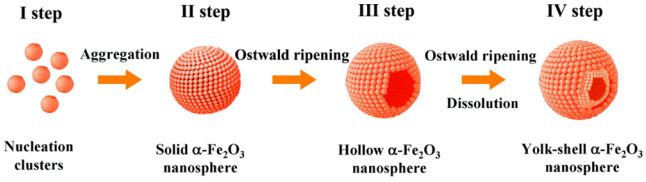

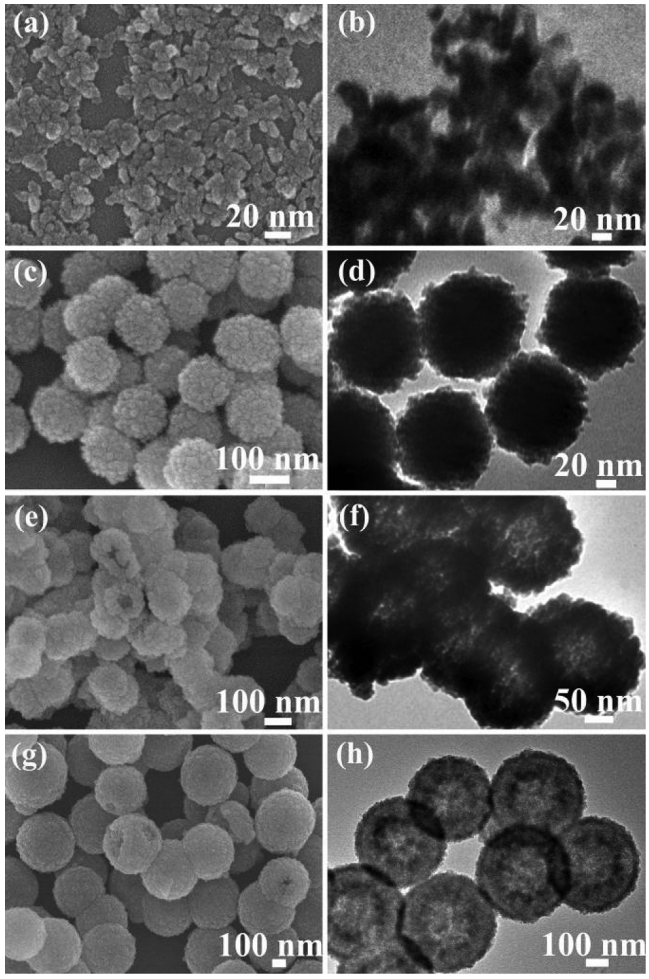

Figure 1. FESEM and TEM images of each step α-Fe_2O_3 products: (a,b) irregular nanoparticles, (c,d) solid nanospheres, (e,f) hollow nanospheres, and (g,h) yolk-shell nanospheres.

DOI: 10.1021/acsami.5b03978
ACS Appl. Mater. Interfaces 2015, 7, 13098–13104

analysis results that the structures of the obtained samples are sensitive to reaction times. With the increase of hydrothermal reaction times, the structures of the sample in each step are first changed from irregular nanoparticles to solid nanospheres, then to hollow nanospheres, and finally formed yolk-shell nanospheres. Therefore, regulation of the reaction time could be a way to understand the morphology change.

Figure 2a–c shows the FESEM images of yolk-shell α-Fe_2O_3 nanospheres, which are made up of uniform monodispersed

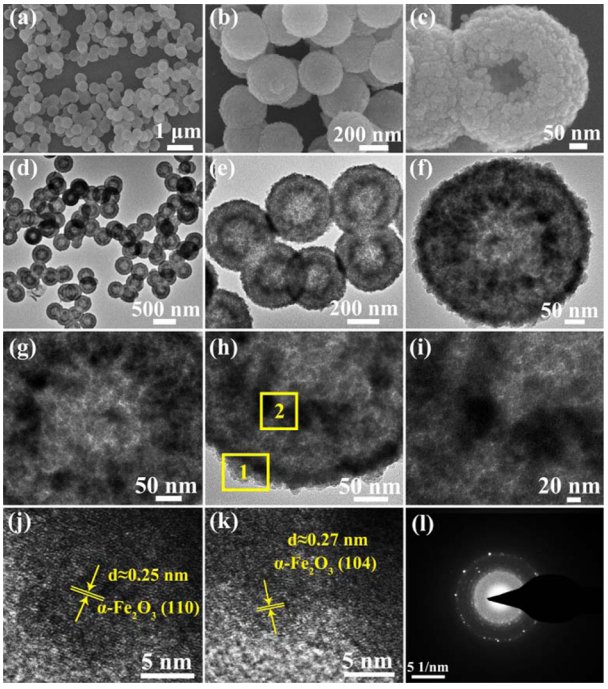

Figure 2. (a–c) Typical FESEM images and (d–i) the low and high-magnification TEM images of the yolk-shell α-Fe_2O_3 nanospheres. (i–k) HRTEM images taken from spots 1 and 2 in (h), respectively, and (l) SAED of the yolk-shell α-Fe_2O_3 nanospheres.

nanospheres. A magnified FESEM image of an individual α-Fe_2O_3 sample in Figure 2c suggests that the diameter of the nanospheres is about 250 nm and the outside surface are loose and rough. Moreover, we have observed a hollow and double shell nanostructure from a broken α-Fe_2O_3 nanosphere, which is further determined via the corresponding low/high-magnification TEM images, as shown in Figure 2d–f. The TEM images (Figure 2d–f) show a potent evidence that the α-Fe_2O_3 nanospheres are made up of hollow nanospheres with double shell (the thicknesses of outer and inner shell layers are about 20 and 40 nm, respectively). The enlargement TEM images of different position of the yolk-shell α-Fe_2O_3 nanospheres from Figure 2f are as Figure 2g–i. Notably, it is clear that there are large amounts of voids and gaps between the adjacent nanoparticles, which indirectly demonstrate the presence of porous structures on each shell of the hollow nanospheres. Figure 2h shows that a distance between outer shell layer and inner shell layer is approximately 50 nm. Particularly, HRTEM images are chosen from the outer and inner shell (Figure 2h) by a yellow square with different numbers inside (Figure 2j,k). Figure 2j (spot 1, Figure 2h) and Figure 2k (spot 2, Figure 2h) show the lattice fringe spacing values of the outer and inner shell are 0.25 and 0.27 nm, which are indexed to the (110) and (104) plane of α-Fe_2O_3 materials, respectively. Furthermore, the yolk-shell α-Fe_2O_3 nanospheres with polycrystalline structures were further determined by the corresponding SAED image (Figure 2l).

The XRD pattern of the yolk-shell α-Fe_2O_3 nanospheres are shown in Figure 3. It is obvious that all of the observed peak

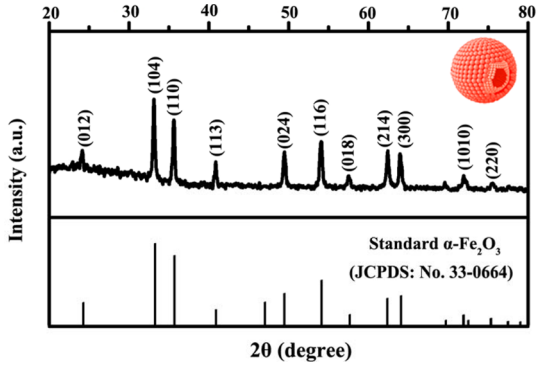

Figure 3. XRD patterns and standard card (JCPDS No. 33-0664) of the yolk-shell α-Fe_2O_3 nanospheres.

positions are in good agreement with the hexagonal structure of the standard card of α-Fe_2O_3 (JCPDS No. 33-0664). The yolk-shell α-Fe_2O_3 nanospheres peaks are relatively sharp in intensity, which indirectly certified that the obtained products by hydrothermal reaction at 200 °C for 30 h has ordinary crystallinity. Moreover, the XRD patterns of other samples including α-Fe_2O_3 nanoparticles, solid nanospheres, hollow nanospheres, and yolk-shell nanospheres are compared in Figure S1 (Supporting Information). It showed that the width decreases and peak intensity increases with the increasing of the reaction time.

The as-synthesized yolk-shell α-Fe_2O_3 nanospheres not only contained a hollow structure but also own porous and loose structures on the surface of the shell layer, which could be favorable for gas diffusion and mass transport in catalytic applications. To further verify the porous structure of the as-synthesized yolk-shell α-Fe_2O_3 nanospheres, nitrogen adsorption–desorption measurement was employed. Figure 4a showed that the BET (Brunauer–Emmett–Teller) surface area of yolk-shell α-Fe_2O_3 nanospheres is 98.3 $m^2\ g^{-1}$. The corresponding pore size distribution curves of yolk-shell α-Fe_2O_3 nanospheres are revealed in the inset of Figure 4a. Most of the pore sizes were calculated to 11.2 nm. Also some other pore size was 95 nm. This formation of pores was largely originated from the hollow interior voids of intraparticles and particularly voids space between the adjacent inside and outside shells. In contrast, the BET and pore-size distribution of other samples (hollow nanospheres, solid nanospheres, and nanoparticles) are displayed in Figure S2a,b (Supporting Information). The specific surface areas of the yolk-shell and hollow nanospheres (98.3 and 81.2 $m^2\ g^{-1}$) are larger than that of the solid nanospheres and nanoparticles (19.7 and 7.8 $m^2\ g^{-1}$), which allows them to absorb more gas molecules. Moreover, Figure 4b shows the EDX analysis of the yolk-shell α-Fe_2O_3 nanospheres, which is mainly composed of Fe and O chemical elements. The peaks of C and Cu elements are from the copper grid. Combined with the analysis result of the XRD pattern (Figure 3), it can be further confirmed that the obtained product was pure phase α-Fe_2O_3 materials.

3.2. Gas Sensing Properties. A series of preparation processes of sensors based on α-Fe_2O_3 samples with irregular

DOI: 10.1021/acsami.5b03978
ACS Appl. Mater. Interfaces 2015, 7, 13098–13104

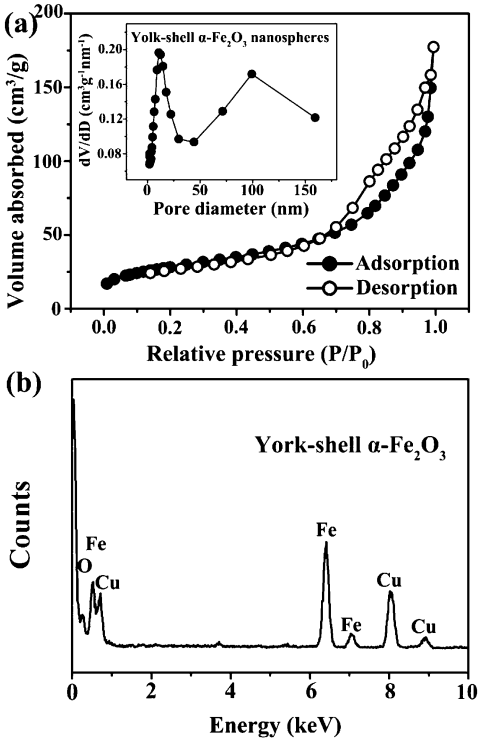

Figure 4. (a) N_2 adsorption−desorption isotherm, BJH pore-size distribution plot (inset), and (b) EDX pattern of the yolk-shell α-Fe_2O_3 nanospheres.

nanoparticles, solid nanospheres, hollow nanospheres, and yolk-shell nanospheres are shown in Figure S3 in the Supporting Information. First, the obtained samples were mixed with moderate amounts of deionized water (about 1/4 weight to the samples), then the samples were coated on a ceramic tube with two Au electrodes to form a sensing layer and finally heat wire (Ni−Cr alloy) was put in the center of the ceramic tube. The specific schematic image and photograph of the device were displayed in parts a and b of Figure 5,

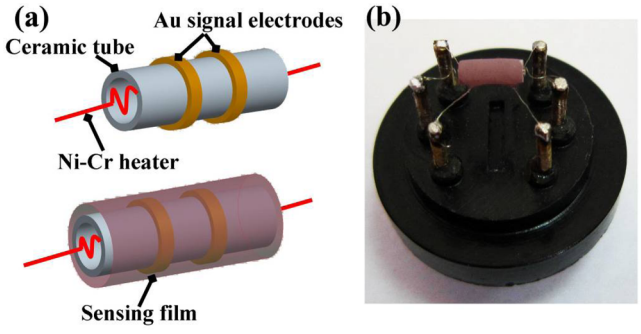

Figure 5. (a) Schematic and (b) photograph images of the α-Fe_2O_3 samples-based sensor.

respectively. The sensing performance of the device was characterized by using a RQ-2 (Qingdao, China) intelligent test meter. For definition of the response (S), the following formula can be used:

$$S = R_a/R_g \quad (2)$$

where R_a represents resistance in the air and R_g represents resistance in target gas. The response/recovery speeds (response/recovery time) were described to reach 90% of the overall resistance change. The detailed definitions for the response and response/recovery time were achieved in our previous work.[20,21]

It is generally known that the effect of the working temperature to sensing performance of metal oxide semiconductor is very large.[8,22] So the relationships between the changing responses of the sensor and the working temperature are first determined. As shown in Figure 6a, it can be observed that all response curves of the sensors exhibit a "parabola"-shape with the raise of temperature in the range from 200 to 280 °C. Notably, when the working temperature is 240 °C, the responses of four sensors can reach to the maximum value. Among them, the yolk-shell α-Fe_2O_3 nanospheres-based sensor revealed about 1.6, 3.0, and 5.0 times enhancement in response (13.4) to 100 ppm ethanol compared to hollow nanospheres (8.2), solid nanospheres (4.4), and irregular nanoparticles (2.7), respectively. These results show that the excellent response of the yolk-shell α-Fe_2O_3 nanospheres-based sensor may attribute to the fantastic multilevel hollow-structure. For Figure 6b−e, resistance values of four sensors are decreased when exposed to reducing gases, which is consistent with gas sensing behaviors of n-type metal oxide semiconductor. Moreover, it can be distinctly observed that the sensor based on the yolk-shell α-Fe_2O_3 nanospheres not only exhibits high response but also has a fast response rate at 240 °C. Table 1 shows the responses and response and recovery times of four samples-based sensors to 100 ppm ethanol. The significantly improved sensing performance (response and response/recovery time) to ethanol in the yolk-shell nanospheres was observed.

Figure 7a shows the dynamic ethanol sensing curve of the sensor based on the yolk-shell α-Fe_2O_3 nanospheres with the concentration in the range from 10 to 100 ppm, which displayed reproducible and reversible sensing behaviors. It can be obviously seen that the sensor based on yolk-shell α-Fe_2O_3 nanospheres have a high response to ethanol. Also the response of the sensor presents a ladder-type improvement as the concentration of ethanol increases. The specific growth trend of the sensor to high concentration of ethanol is shown in Figure 7b. The sensing response of the sensor increases quickly from 10 to 100 ppm (inset Figure 7b) of ethanol gases while the concentration over 500 ppm, the response is increasingly relaxed. However, the response of the sensor gradually reaches saturation when the concentration of ethanol exceeds 1000 ppm. One possible reason is that the sensing response of the sensor highly depends on the removal of oxygen ions via reaction with the target gas. With the concentration increasing, a mass of target gases were covered on the surface of the sensing materials leading to a lower surface reaction that occurred. So, the increase speed of the response became slow.

The fast response and recovery time is playing a vital role for real-time detection of toxic gases in the field of gas sensors. Figure 8a shows that the response (recovery) times of the sensor based on the yolk-shell α-Fe_2O_3 nanospheres to 10, 20, 50, 80, and 100 ppm are 3.0 (17.0), 2.5 (12.0), 1.8 (10.0), 1.1 (8.2), and 0.5 s (7.0 s), respectively. The fast response time (0.5 s for 100 ppm ethanol) is attributed to the yolk-shell nanospheres with a porous shell (Figure 4a), and it is the fastest value reported in the literature for α-Fe_2O_3 sensors (Table 2).[3,11,23−25] In order to further consider the application value of the obtained sensor, a comparison about the sensing ability of the sensor based on the yolk-shell α-Fe_2O_3

DOI: 10.1021/acsami.5b03978
ACS Appl. Mater. Interfaces 2015, 7, 13098−13104

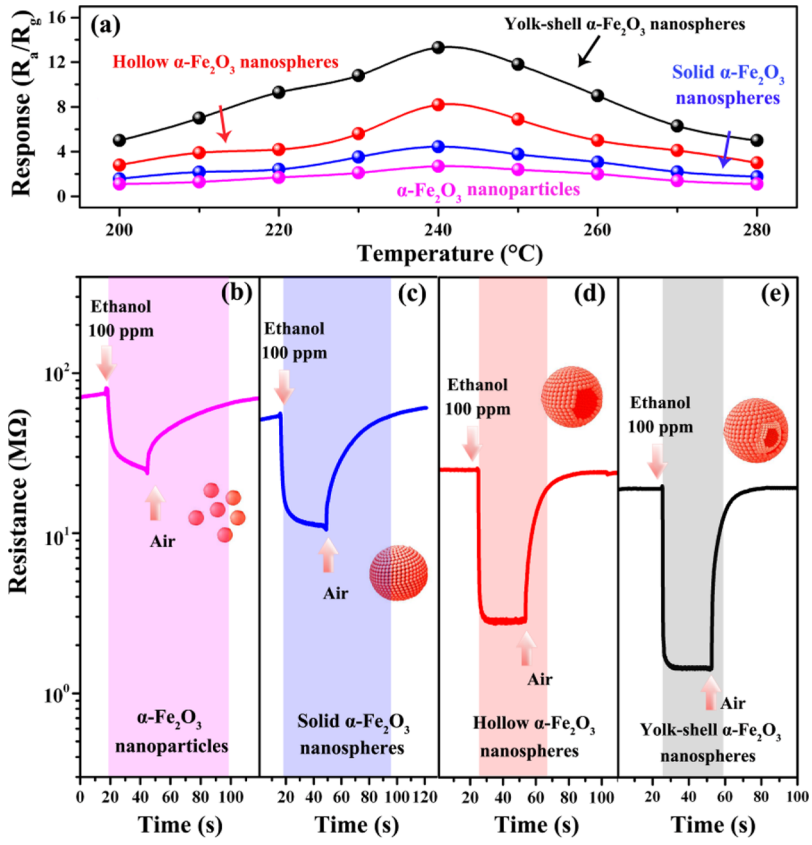

Figure 6. (a) Relationship of responses vs the working temperature and (b–e) response transients (240 °C) of four sensors to 100 ppm ethanol.

Table 1. Comparison of the Response and Response/Recovery Times of Four Sample-Based Sensors

sample	concn	response time/τ_{res}	recovery time/τ_{recov}	response
α-Fe_2O_3 nanoparticles	100 ppm ethanol	11 s	56 s	2.7
solid α-Fe_2O_3 nanospheres	100 ppm ethanol	6 s	48 s	4.4
hollow α-Fe_2O_3 nanospheres	100 ppm ethanol	2 s	17 s	8.2
yolk-shell α-Fe_2O_3 nanospheres	100 ppm ethanol	0.5 s	7 s	13.4

nanospheres to various reducing gases are researched and displayed in Figure 8b. It can be found that the response values of the sensor to 100 ppm of C_2H_5OH, CH_3OH, C_3H_6O, CO, and H_2S at 240 °C are 13.4, 3.1, 4.5, 1.3, and 2.1, respectively. However, it is known that the different gases have different optimum operating temperatures. For the working temperature at 240 °C, the yolk-shell α-Fe_2O_3 nanospheres-based sensor shows a high ethanol sensing response, which is about 3.0–10.3 times in response to that of other gases (CH_3OH, C_3H_6O, CO, and H_2S).

Figure 9 shows the long-term stability of the yolk-shell α-Fe_2O_3 nanosphere-based sensors to 100 ppm ethanol at different working temperatures. It can be easily seen that all of the ethanol-sensing responses of the yolk-shell α-Fe_2O_3 nanosphere-based sensors at working temperatures from 240 to 320 °C decreased about 5% as time increased from 1 to 30 days. Thus, the yolk-shell α-Fe_2O_3 nanosphere-based sensors displayed an excellent long-term stability.

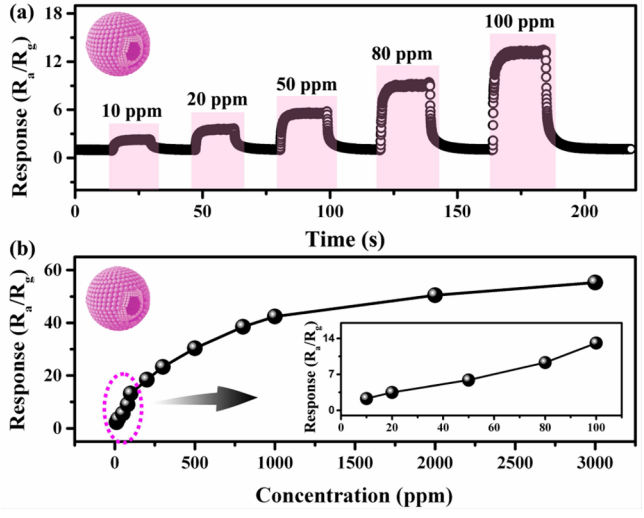

Figure 7. (a) Dynamic sensing response of the yolk-shell α-Fe_2O_3 nanospheres to 10–100 ppm of ethanol at 240 °C and (b) the relationship of response vs the ethanol concentration (inset response of the sensor to 10–100 ppm ethanol).

3.3. Gas Sensing Mechanism of the Yolk-Shell α-Fe_2O_3 Nanospheres. For now, large studies indicate that the properties of gas sensors have strong dependence on the material's morphology or shape.[8,22–26] However, in our work, the improved ethanol sensing properties of the sensor based on the yolk-shell α-Fe_2O_3 nanospheres are primarily due to the perfect architecture, i.e., hollow structure with the porous double shell (Figure 2). It is very well-known that such yolk-shell nanospheres own a protective hollow shell, in which a

DOI: 10.1021/acsami.5b03978
ACS Appl. Mater. Interfaces 2015, 7, 13098–13104

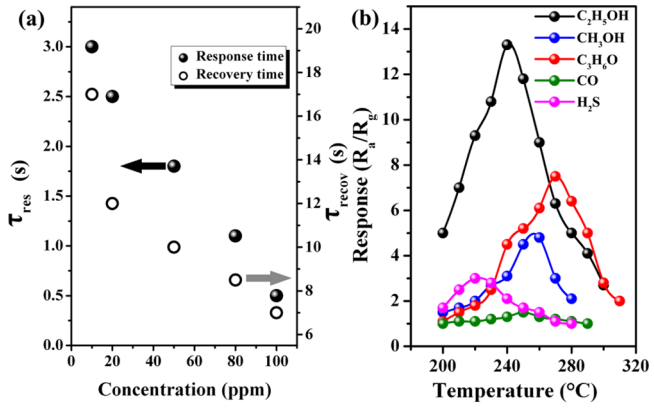

Figure 8. (a) Response/recovery time of the yolk-shell α-Fe_2O_3 nanosphere-based sensor to 10−100 ppm ethanol at 240 °C and (b) selectivity of the yolk-shell α-Fe_2O_3 nanosphere-based sensor to 100 ppm of various gases at different working temperatures.

Table 2. Ethanol Response Times of the α-Fe_2O_3 Nanomaterials-Based Gas Sensors[a]

materials	size/nm	ethanol concn/ppm	temp /°C	τ_{res}/s	ref
this work	~250	100	240	0.5	
flower-like α-Fe_2O_3	5−6 μm	100	280	1.0	3
sheet-like α-Fe_2O_3	500	100	250	5.0	11
hollow α-Fe_2O_3	2−4.5 μm	100	350	21.0	23
α-Fe_2O_3 microcubes	1 μm	50	320	6.0	24
α-Fe_2O_3 nanobelts	400	100	350	10.0	25

[a]concn, concentration; temp, temperature; τ_{res}, response time; ref, references

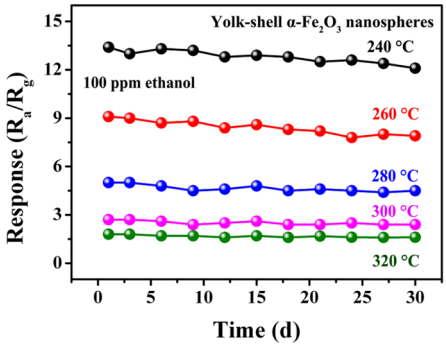

Figure 9. Long-term stability of the yolk-shell α-Fe_2O_3 nanosphere-based sensor to 100 ppm ethanol at 240, 260, 280, 300, and 320 °C, respectively.

small hollow core is encapsulated. First, the outer shell layer could not only availably separate hollow core nanospheres but prevent them from aggregating.[4,8] Also the outer shell layer possesses a porous structure, and these porous structures can offer a sufficiently active surface and good permeability to gas adsorption and gas diffusion.[27] On the other side, the inner shell possesses a hollow structure and it has a larger specific surface areas. The high response may be due to the larger specific surface areas of the yolk-shell and hollow nanospheres (98.3 m^2 g^{-1}), which allows the outer and inner surface to absorb more target gases. So, when the sensor based on yolk-shell α-Fe_2O_3 nanospheres was exposed to air (Figure 10a), a mass of oxygen molecules were absorb on the surface of inner

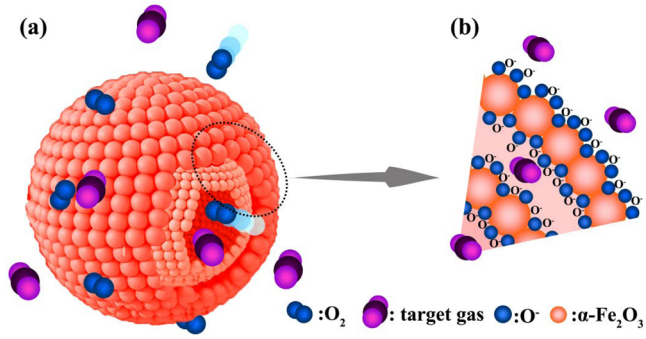

Figure 10. (a) Schematic diagram of possible gas sensing mechanisms of the yolk-shell nanospheres and (b) a portion of the yolk-shell nanospheres.

and outer shell layer of the nanospheres to form oxygen ions (O^- or O^{2-}), leading to a greater of electron depletion layer from inner and outer surface of the yolk-shell α-Fe_2O_3 nanospheres (Figure 10b).[28] When ethanol was introduced and reacted with oxygen ions, the electrons quickly back to basis material to cause a large change in electrical conductivity of the yolk-shell structure. Thus, the high response was obtained. Furthermore, the shell layer possesses a porous structure. Such pores with a diameter of about 11.2 nm and gap developed to accelerate the in-diffusion of the target gases toward the materials surfaces, then enhancing the response rate. It hence reveals a large amount of enhanced performances compared to conventional solid and hollow structured nanomaterials.

4. CONCLUSIONS

In conclusion, well-defined yolk-shell α-Fe_2O_3 nanospheres were synthesized by a hydrothermal route. The peculiarity of the morphology is that, the thickness of the outer shell layer of α-Fe_2O_3 hollow nanospheres is about 20 nm with a hollow nanospheres core of about 200 nm. The different structure (irregular nanoparticles, solid nanospheres, and hollow nanospheres) of α-Fe_2O_3 materials were successfully achieved by adjusting different reaction times. Four different structures of sensing materials were used as gas sensors. Dramatically, a high response (13.4) and fast response time (0.5 s) to 100 ppm of C_2H_5OH was obtained in yolk-shell α-Fe_2O_3 nanosphere-based sensors. It exhibited about 3.0−10.3-fold higher C_2H_5OH response compared to the other ones. Thus, this fantastic multilevel structure may be a good wealth of outstanding property applications in chemical sensors.

■ ASSOCIATED CONTENT

Supporting Information

XRD patterns of the as-synthesized α-Fe_2O_3 samples, N_2 adsorption−desorption isotherm and BJH pore-size distribution plot of the assynthesized α-Fe_2O_3 samples, and preparation processes of sensors based on α-Fe_2O_3 samples.The Supporting Information is available free of charge on the ACS Publications website at DOI: 10.1021/acsami.5b03978.

DOI: 10.1021/acsami.5b03978
ACS Appl. Mater. Interfaces 2015, 7, 13098−13104

AUTHOR INFORMATION

Corresponding Author

*E-mail: zhangtong@jlu.edu.cn. Phone: +86 431 85168385. Fax: +86 431 85168270.

Notes

The authors declare no competing financial interest.

ACKNOWLEDGMENTS

This research work was financially supported by the Postdoctoral Science Foundation of China (No. 2015M571361), Graduate Innovation Fund of Jilin University (Grant No. 2014093), and Program for Chang Jiang Scholars and Innovative Research Team in University (Grant No. IRT13018). The authors thank Tingting Zhou, for sensor stability measure experimental assistance and useful discussions.

REFERENCES

(1) Williams, D. E. Semiconducting Oxides as Gas-Sensitive Resistors. *Sens. Actuators, B* **1999**, *57*, 1−16.

(2) Kim, H. R.; Choi, K. I.; Kim, K. M.; Kim, I. D.; Cao, G. Z.; Lee, J. H. Ultra-Fast Responding and Recovering C_2H_5OH Sensors Using SnO_2 Hollow Spheres Prepared and Activated by Ni Templates. *Chem. Commun.* **2010**, *46*, 5061−5063.

(3) Wang, L. L.; Fei, T.; Lou, Z.; Zhang, T. Three-Dimensional Hierarchical Flowerlike α-Fe_2O_3 Nanostructures: Synthesis and Ethanol-Sensing Properties. *ACS Appl. Mater. Interfaces* **2011**, *3*, 4689−4694.

(4) Zhao, Y.; Jiang, L. Hollow Micro/Nanomaterials with Multilevel Interior Structures. *Adv. Mater.* **2009**, *21*, 3621−3638.

(5) Zhong, J. Y.; Cao, C. B.; Liu, H.; Ding, Y. L.; Yang, J. Fabrication of Hollow and Yolk−Shell Structured η-Fe_2O_3 Nanoparticles with Versatile Configurations. *Ind. Eng. Chem. Res.* **2013**, *52*, 1303−1308.

(6) Wang, Z. Y.; Zhou, L.; Lou (David), X. W. Metal Oxide Hollow Nanostructures for Lithium-ion Batteries. *Adv. Mater.* **2012**, *24*, 1903−1911.

(7) Wang, L. L.; Lou, Z.; Fei, T.; Zhang, T. Zinc Oxide Core−Shell Hollow Microspheres with Multi-shelled Architecture for Gas Sensor Applications. *J. Mater. Chem.* **2011**, *21*, 19331−19336.

(8) Wang, L. L.; Dou, H. M.; Lou, Z.; Zhang, T. Encapsuled Nanoreactors (Au@SnO_2): A New Sensing Material for Chemical Sensors. *Nanoscale* **2013**, *5*, 2686−2691.

(9) Liu, J.; Qiao, S. Z.; Hu, Q. H.; Lu (Max), G. Q. Magnetic Nanocomposites with Mesoporous Structures: Synthesis and Applications. *Small* **2011**, *7*, 425−443.

(10) Lee, J. H. Gas Sensors Using Hierarchical and Hollow Oxide Nanostructures: Overview. *Sens. Actuators, B* **2009**, *140*, 319−336.

(11) Hao, Q. Y.; Liu, S.; Yin, X. M.; Du, Z. F.; Zhang, M.; Li, L. M.; Wang, Y. G.; Wang, T. H.; Li, Q. H. Flexible Morphology-Controlled Synthesis of Mesoporous Hierarchical a-Fe_2O_3 Architectures and Their Gas-Sensing Properties. *CrystEngComm* **2011**, *13*, 806−812.

(12) Li, X. L.; Wei, W. J.; Wang, S. Z.; Kuai, L.; Geng, B. Y. Single-Crystalline a-Fe_2O_3 Oblique Nanoparallelepipeds: High-Yield Synthesis, Growth Mechanism and Structure Enhanced Gas-Sensing Properties. *Nanoscale* **2011**, *3*, 718−724.

(13) Lian, J. B.; Duan, X. C.; Ma, J. M.; Peng, P.; Kim, T.; Zheng, W. J. Hematite (a-Fe_2O_3) with Various Morphologies: Ionic Liquid−Assisted Synthesis, Formation Mechanism, and Properties. *ACS Nano* **2009**, *3*, 3749−3761.

(14) Sun, Z. Y.; Xie, K. P.; Li, Z. A.; Sinev, I.; Ebbinghaus, P.; Erbe, A.; Farle, M.; Schuhmann, W.; Muhler, M.; Ventosa, E. Hollow and Yolk-Shell Iron Oxide Nanostructures on Few-Layer Graphene in Li-Ion Batteries. *Chem.—Eur. J.* **2014**, *20*, 2022−2030.

(15) Son, M. Y.; Hong, Y. J.; Lee, J. K.; Kang, Y. C. One-Pot Synthesis of Fe_2O_3 Yolk−Shell Particles with Two, Three, and Four Shells for Application as An Anode Material in Lithium-Ion Batteries. *Nanoscale* **2013**, *5*, 11592−11597.

(16) Lai, X. Y.; Li, J.; Korgel, B. A.; Dong, Z. H.; Li, Z. M.; Su, F. B.; Du, J.; Wang, D. General Synthesis and Gas-Sensing Properties of Multiple-Shell Metal Oxide Hollow Microspheres. *Angew. Chem., Int. Ed.* **2011**, *50*, 2738−2741.

(17) Zhang, H. G.; Zhu, Q. S.; Zhang, Y.; Wang, Y.; Zhao, L.; Yu, B. One-Pot Synthesis and Hierarchical Assembly of Hollow Cu_2O Microspheres with Nanocrystals-Composed Porous Multishell and Their Gas-Sensing Properties. *Adv. Funct. Mater.* **2007**, *17*, 2766−2771.

(18) Ma, J.; Zhang, X. D.; Chen, K. Z.; Li, G. C.; Han, X. D. Morphology-Controlled Synthesis of Hematite Hierarchical Structures and Their Lithium Storage Performances. *J. Mater. Chem. A* **2013**, *1*, 5545−5553.

(19) Huo, Y.; Zhu, Y. G.; Xie, J.; Cao, G. S.; Zhu, T. J.; Zhao, X. B.; Zhang, S. C. Controllable Synthesis of Hollow a-Fe_2O_3 Nanostructures, Their Growth Mechanism, and The Morphology-Reserved Conversion to Magnetic Fe_3O_4/C Nanocomposites. *RSC Adv.* **2013**, *3*, 19097−19103.

(20) Wang, L. L.; Lou, Z.; Fei, T.; Zhang, T. Templating Synthesis of ZnO Hollow Nanospheres Loaded with Au Nanoparticles and Their Enhanced Gas Sensing Properties. *J. Mater. Chem.* **2012**, *22*, 4767−4771.

(21) Wang, L. L.; Deng, J. N.; Lou, Z.; Zhang, T. Cross-Linked p-type Co_3O_4 Octahedral Nanoparticles in 1D n-type TiO_2 Nanofibers for High-Performance Sensing Devices. *J. Mater. Chem. A* **2014**, *2*, 10022−10028.

(22) Zhang, J.; Liu, X. H.; Wu, S. H.; Xu, M. J.; Guo, X. Z.; Wang, S. R. Au Nanoparticle-Decorated Porous SnO_2 Hollow Spheres: A New Model for A Chemical Sensor. *J. Mater. Chem.* **2010**, *20*, 6453−6459.

(23) Zhang, F. H.; Yang, H. Q.; Xie, X. L.; Li, L.; Zhang, L. H.; Yu, J.; Zhao, H.; Liu, B. Controlled Synthesis and Gas-Sensing Properties of Hollow Sea Urchin-Like α-Fe_2O_3 Nanostructures and α-Fe_2O_3 Nanocubes. *Sens. Actuators, B* **2009**, *141*, 381−389.

(24) Xiong, S.; Xu, J.; Chen, D.; Wang, R. M.; Hu, X. L.; Shen, G. Z.; Wang, Z. L. Controlled Synthesis of Monodispersed Hematite Microcubes and Their Properties. *CrystEngComm* **2011**, *13*, 7114−7120.

(25) Fan, H. T.; Zhang, T.; Xu, X. J.; Lv, N. Fabrication of N-type Fe_2O_3 and P-type $LaFeO_3$ Nanobelts by Electrospinning and Determination of Gas-sensing Properties. *Sens. Actuators, B* **2011**, *153*, 83−88.

(26) Chang, Y. E.; Youn, D. Y.; Ankonina, G.; Yang, D. J.; Kim, H. G.; Rothschild, A.; Kim, I. D. Fabrication and Gas Sensing Properties of Hollow SnO_2 Hemispheres. *Chem. Commun.* **2009**, 4019−4021.

(27) Hu, P.; Han, N.; Zhang, X.; Yao, M. S.; Cao, Y. B.; Zuo, A. H.; Yang, G.; Yuan, F. L. Fabrication of ZnO Nanorod-Assembled Multishelled Hollow Spheres and Enhanced Performance in Gas Sensor. *J. Mater. Chem.* **2011**, *21*, 14277−14284.

(28) Wang, L. L.; Fei, T.; Deng, J. N.; Lou, Z.; Wang, R.; Zhang, T. Synthesis of Rattle-Type SnO_2 Structures with Porous Shells. *J. Mater. Chem.* **2012**, *22*, 18111−18114.

DOI: 10.1021/acsami.5b03978
ACS Appl. Mater. Interfaces 2015, 7, 13098−13104